Transmission electron microscopy of thiol-capped Au clusters on C: structure and electron irradiation effects

Lionel C. Gontard[a,*] and Rafal E. Dunin-Borkowski[b]

[a] *Instituto de Ciencia de Materiales de Sevilla (CSIC), 41092, Sevilla, Spain*

[b] *Ernst Ruska-Centre for Microscopy and Spectroscopy with Electrons and Peter Grünberg Institute, Forschungszentrum Jülich, D-52425 Jülich, Germany*

Keywords: in situ TEM, electron irradiation, amorphous C, thiol-protected clusters, Au clusters, Au atoms, graphene, graphite, tribology

** email: lionel.cervera@icmse.csic.es/lionelcg@gmail.com. Phone: +34 954489576*

Abstract

High-resolution transmission electron microscopy is used to study interactions between thiol-capped Au clusters and amorphous C support films. The morphologies of the clusters are found to depend both on their size and on the local structure of the underlying C. When the C is amorphous, larger Au clusters are crystalline, while smaller clusters are typically disordered. When the C is graphitic, the Au particles adopt either elongated shapes that maximize their contact with the edge of the C film or planar arrays when they contain few Au atoms. We demonstrate the influence of electron beam irradiation on the structure, shape and stability of the Au clusters, as well as on the formation of holes bounded by terraces of graphitic lamellae in the underlying C.

1 Introduction

A fundamental atomic-scale understanding of the size-dependent structure and stability of Au and thiol-capped Au clusters on C allotropes (e.g., amorphous C, graphite and graphene) is important for their controlled synthesis for applications in catalysis (Li *et al.,* 2010), nanomedicine and chemical and biological sensing (Saha *et al.,* 2012; Daniel and Astruc, 2004). Although the phase diagrams of nanoparticles and clusters can be predicted theoretically based on thermodynamics, such calculations cannot easily be used to predict nanoparticle shapes that result from kinetic considerations and they usually do not consider the role of the support (Barnard *et al.,* 2009; Kuwauchi et al., 2013; Gontard *et al.,* 2014).

Here, we study the size-dependent properties of Au clusters supported on amorphous C (a-C) films at the atomic scale using high-resolution transmission electron microscopy (HRTEM). In recent years, aberration-corrected HRTEM has been successfully combined with *ab initio* calculations to study the binding sites and energies of single atoms on graphene (Meyer *et al.,* 2008; Boukhvalov and Katsnelson, 2009; Cretu *et al.,* 2010; Vanin *et al.,* 2010; Zan *et al.,* 2012; Ramasse *et al.,* 2012; Wang *et al.,* 2012a , 2012b, 2013; Hardcastle *et al.,* 2013), Ostwald ripening between mono- and bi- metallic nanoparticles on a-C (Yoshida *et al.,* 2012, 2013; Alloyeau *et al.,* 2012), the diffusion of metal atoms and clusters on a-C, graphene and C nanotubes (Werner *et al.,* 2005; Wanner *et al.,* 2006; Batson, 2008; Gan *et al.,* 2008; Cretu *et al.,* 2010, 2012) and the diffusion and etching of clusters on graphene (Booth *et al.,* 2011; Wang *et al.,*2012b, 2013). Aberration-corrected HRTEM and density functional theory have also been used to investigate the structures of thiol-protected clusters (Mariscal *et al.,* 2010).

In HRTEM studies, the effect of irradiation by highly energetic electrons must be taken into account (Egerton *et al.*, 2004; Gontard *et al.*, 2012). In particular, the energy supplied by an electron in an elastic collision can displace an atom (knock-on) if the maximum energy transferred is higher than the threshold energy for removing the atom from its site. Electron irradiation can also rearrange the structures of C allotropes, even resulting in the irradiation-induced transformation of graphite to diamond (Krasheninnikov and Banhart, 2007; Borrnërt *et al.,* 2012; Girit *et al.,* 2009; Zhu *et al.,* 2012).

Here, we use aberration-corrected HRTEM and multislice simulations to study Au clusters on an a-C film. We correlate the kinetic shapes adopted by small Au and thiol-protected Au clusters with the local structure of the underlying C and discuss electron-beam-induced changes of the a-C (including the formation of graphitic terraces).

2. Methods

2.1 Sample preparation

Au nanoparticles capped with dodecanethiols (Au-SR), the radical R being $-(CH_2)_{11}-CH_3$, were synthesized by liquid-liquid phase reduction at room temperature using the method of Brust *et al.* (1994). Dodecanethiols are alkane chains, i.e., organic compounds made of chains of C and H that bond to the surface of Au through a S atom. Drops of the colloidal Au-SR nanoparticles were dissolved in water, deposited onto ultrathin C films supported on TEM grids supplied by *Ted Pella* and dried in air. The thicknesses of the a-C films were estimated to be 16 nm by assuming an electron-beam-induced sputtering rate at their exit surface of 0.09 nm/s (see Supporting Information).

2.2 Sample characterisation

HRTEM images were acquired at 300 kV using an aberration-corrected FEI Titan TEM equipped with a high brightness field emission gun and a 2048 × 2048 pixel charge-coupled-device (CCD) Ultrascan camera with 2× binning and acquisition times of between 0.5 and 2 s. Aberrations were measured by acquiring defocus/beam tilt tableaux as a function of radial and azimuthal beam tilt angle. The spherical aberration coefficient (C_S) was adjusted to a value of -4.5 µm. High-angle annular dark-field scanning TEM (HAADF STEM) images were acquired at 300 kV using a probe-corrected FEI Titan TEM equipped with a high brightness field emission gun. The value of C_S was adjusted to -30 µm and a probe convergence semi-angle of 19 mrad and a collection semi-angle of 75 mrad were used.

2.3 Image simulation

Simulations of HRTEM images were performed using the multislice algorithm in *JEMS* software, with the transfer function of the microscope incorporated using the parameters listed in Table S1, which were chosen to provide a match to the experimentally observed contrast. 1% random noise was added to the final simulations, which were also low-pass filtered to simulate the effect of the modulation transfer function of the CCD camera. The effect of electron-optical aberrations, particularly defocus and astigmatism, was included. The Debye-Waller factor used was 0.005 nm^2. The simulations were based on atomistic models generated using a dedicated software program written in *Matlab*. Models of an a-C film were obtained by starting from a hypothetical C crystal comprising a cubic structure with one C atom at each corner of the unit cell. The unit cell dimension was chosen to be 150 pm to match the average C-C bond length. The position of each atom was changed from its starting value by a random number multiplied by 30% of the unit cell dimension. This model was then refined by creating holes and deleting atoms selectively until the structure resembled that observed in experimental images.

3. Results and discussion

3.1. Structures of Au clusters

Fig. 1 shows representative HRTEM and atomic-resolution HAADF STEM images of Au-RS clusters on a-C recorded at room temperature. The larger particles are crystalline, whereas particles that are smaller than about 1.5 nm do not have well-defined crystalline structures. Both chains of Au atoms with unusual Au-Au distances and isolated Au atoms are observed close to the edges of the particles, irrespective of their size (see Movies S1-S4), while isolated Au atoms are also distributed across the film. Although it is tempting to associate the rough surfaces of some of the particles with the thiol molecules (Mariscal *et al.*, 2010; Luedtke and Landman, 1996; Kaushik and Clancy, 2012), the low atomic numbers of the atoms in the molecules and the high contrast of the C support suggest that they are not readily visible.

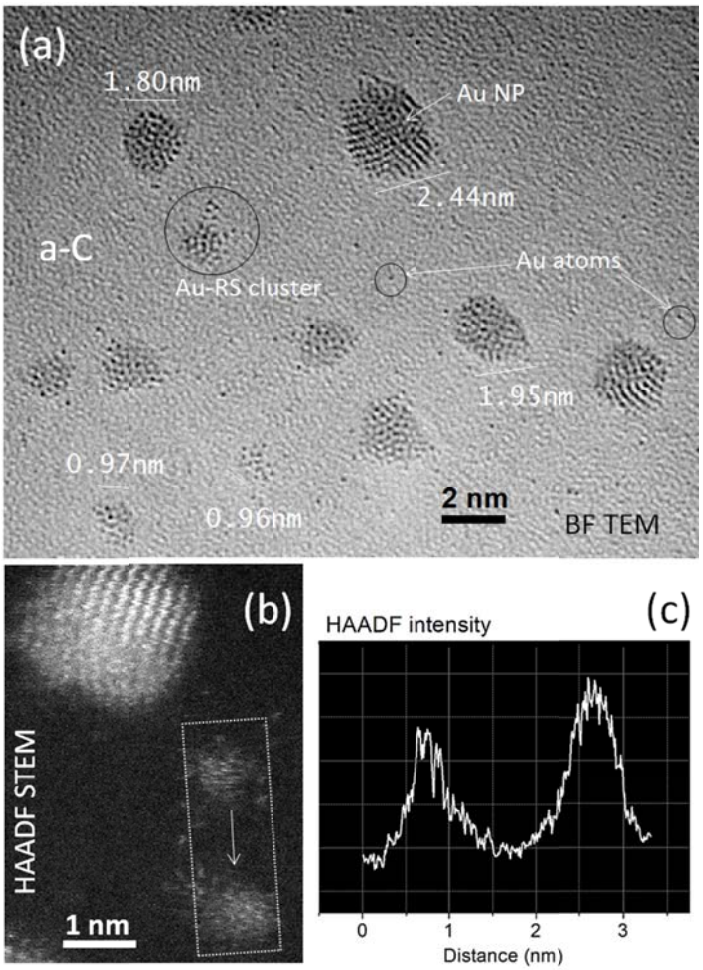

Fig. 1 (a) HRTEM image of Au clusters capped with thiols supported on amorphous carbon. Larger cluster are crystalline, while clusters with sizes below about 1.5 nm are more disordered. During electron irradiation, smaller clusters undergo significant atomic rearrangement. Individual Au atoms (dark dots) are also scattered on the support film. Most clusters have irregular surfaces and are surrounded by atoms that are not part of their surface but "linked" to them. (b) Atomic-resolution HAADF STEM image showing Au atoms that are either scattered on the C film or attached to the particles with unusual Au-Au distances (circles). (c) The HAADF intensity profile integrated inside the square shown in (b) shows that the clusters are not planar.

Fig. 2 shows a series of frames taken from a movie of nanoparticles and clusters undergoing changes during irradiation at an electron dose rate of 46 A/cm^2 (2.9x10^6 electrons/nm^{2}s) (see Movie S1). Due to the presence of the electron beam, the alkyl chains in the thiols and atoms at the S/Au interfaces are thought to undergo dissociation of C-H, C-C, C-S and Au-thiolate bonds, increasing cross-linking between the chains and forming unsaturated hydrocarbons through C=C double bond formation (Zharnikov *et al.*, 1999). The formation, aggregation and annealing of defects in the Au particles and the a-C film are determined by the energy of the electron beam and the binding and migration energies of Au, S and C (see Tables S2 - S4). 300 kV electrons can transfer up to 4.3 eV to a Au atom, 26.6 eV to a S atom and 70.9 eV to a C atom. These energies are sufficient to result in depinning of Au atoms, evaporation of Au and S atoms from clusters, breaking of C-C and Au-S bonds, sputtering of C and the rearrangement of smaller clusters. The crystalline configurations of larger clusters make them more radiation-hard

because an energy of 34 eV is needed to knock-on one Au atom into an interstitial site. Although the increase in specimen temperature due to the electron beam is expected to be low for the conditions used in our experiments (Egerton *et al.*, 2004), an electron-beam-induced increase in temperature resulting, for example, from the emission of Auger electrons can lead to enhanced mobility of surface atoms and easier removal by sputtering or evaporation (Williams, 1987). For instance, the energy barrier for evaporating atoms from a Au nanoparticle surface onto the support is at least E_a-E_c=3.5 eV, where E_a is the adsorption energy of a Au adatom (0.3 eV on a-C) and E_c is the cohesive energy of the Au nanoparticle (Wenner *et al.*, 2005; Wanner *et al.*, 2006). The value of E_c for a Au cluster is predicted to increase with particle size, taking values of between 1.2 eV/atom for two Au atoms and 3.8 eV/atom for a bulk crystal (Chan and Yim, 2013). Hence, the smallest clusters are expected to be more unstable under electron irradiation.

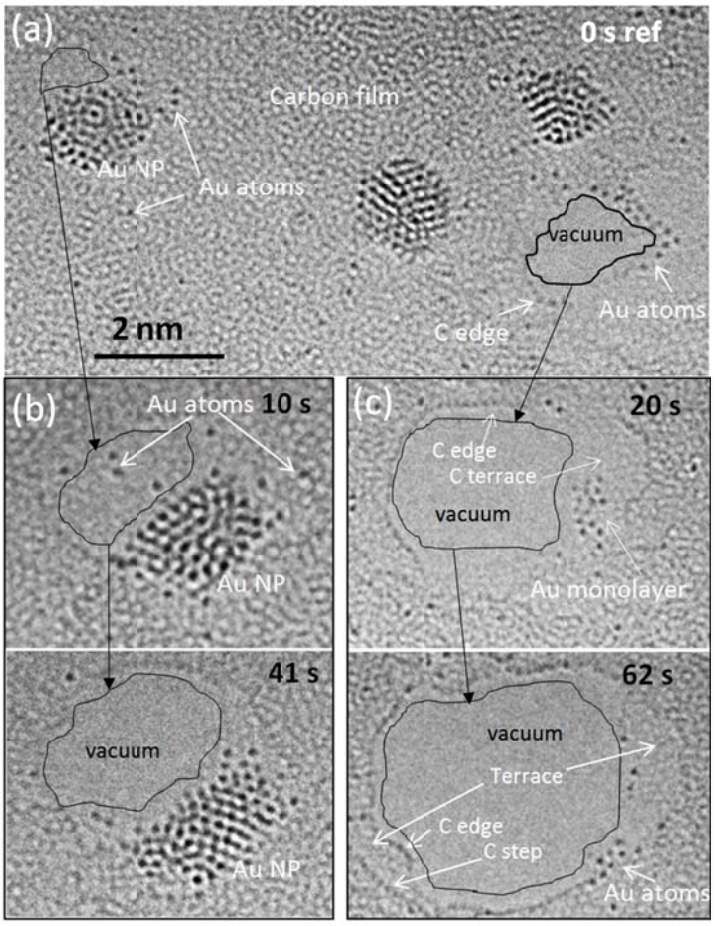

Fig. 2 Frames taken from Movie S1, showing transformations of the sample during electron beam irradiation at a dose rate of 46 A/cm^2. (a) Opening of holes in the a-C film; (b) A cluster interacting with the edge of the C, changing its shape to match that of the hole; (c) A hole enlarging and graphitic terraces forming on opposite sides of it, with Au atoms forming closed-packed monolayers on the graphite edges.

Movies S1-S4 show that Au clusters (particularly smaller ones) fluctuate continuously between ordered and disordered configurations. This phenomenon has been observed in many TEM experiments and has stimulated debate about whether such fluctuations are primarily electron-beam-activated or whether they are associated with an intrinsic quasimelting state of small clusters (Smith *et al.*, 1986; Ajayan and

Marks, 1989). *Ab initio* studies predict that the most stable configuration of an unsupported 10-20 atom Au cluster is amorphous and that the energy difference between different atomic configurations is very small, supporting the concept of quasimelting (Wang *et al.*, 2002; Chan and Yim, 2013). Moreover, S atoms from the thiols may remain bonded to the surfaces of the nanoparticles because the Au-S bond has a strength close to that of the Au-Au bond (Häkkinen, 2012) and can also modify Au-Au bonds at the particle surface (see Table . In this way, at 300 K a competition between perpendicular (Au-S) and lateral (Au-Au) bonding is expected to distort the structures of smaller thiol-capped clusters (Mariscal *et al.*, 2010).

3.2. Multislice simulations

Figs. 3 and 4 show the results of multislice simulations performed to interpret the contrast features in the HRTEM images. Fig. 3 shows a comparison of an experimental image (Fig. 3a) with a simulated image (Fig. 3b) calculated using the atomistic model shown in Fig. 3c. The model comprises a crystalline Au particle with a size of 1.5 nm supported on an a-C film that has a thickness of 5 nm. The model also contains 10 Au atoms (only 8 of which are visible in the x-y projection), which are distributed both within the a-C film and on its surface. Although many of the features in the experimental image are reproduced in the simulated image, the experimental contrast is lower than that in the simulation when the intensities in the experimental and simulated images are both normalized to the same intensity in vacuum (Howie, 2004).

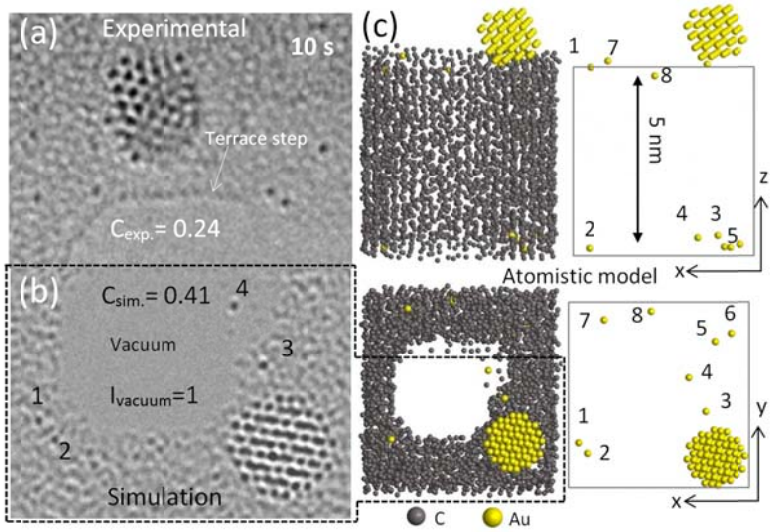

Fig. 3 (a) Detail of experimental HRTEM image of a Au cluster on a-C, a terrace step, a patch of graphite and isolated Au atoms. (b) Multislice simulation performed using the model shown in (c). The simulation shows that the apparent size and the details of the contrast associated with a Au atom depend strongly on its location. The simulated contrast is approximately twice that of the experimental contrast when the images are normalized to the same intensity in vacuum.

The simulation in Fig. 3b shows that individual Au atoms can be identified in an HRTEM image wherever they are located in the C support film (see, e.g., atoms 1 and 2). However, the symmetry of the contrast

associated with an individual Au atom, which reflects both the imaging conditions and the bonding of the atom, depends on the atoms in its neighborhood and also on the aberrations of the imaging system (Meyer et al., 2011, Ciston *et al.*, 2011). Even a small amount of two-fold astigmatism and defocus is able to change the shape and symmetry of the contrast associated with a Au atom significantly. Atom 4 in Fig. 3b, which is the only Au atom in the simulation that does not have C atoms above or below it, displays contrast with circular symmetry. The simulations in Fig. 4 confirm the experimental observation that the apparent size of a Au atom can change as a function of its defocus (i.e., its position in the electron beam direction).

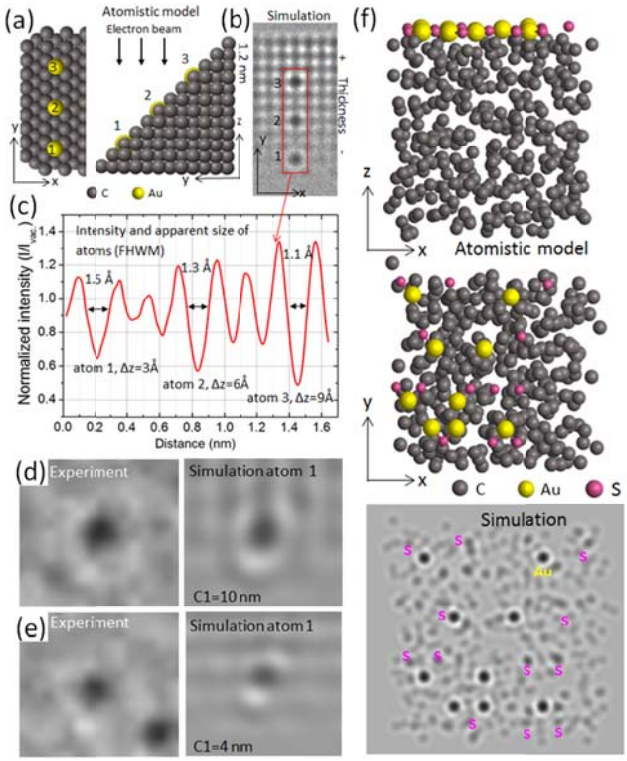

Fig. 4 (a) Model of a wedge-shaped crystal of C with three Au atoms at different heights. The wedge has the same density as that of amorphous C but takes the form a simple artificial crystalline structure here as its purpose is only to illustrate the difference between its contrast and that of Au atoms placed at different heights. (b) Corresponding multislice simulation showing that the contrast of the Au atoms depends on their position and on the thickness of the film. (c) Line profile of the intensities in the simulated image normalized to the intensity in vacuum in (b), showing different apparent diameters of the Au atoms. (d) and (e) Experimental images of Au atoms compared with multislice simulations calculated using the parameters given in Table S1, showing that the details of the image contrast change rapidly when the defocus C1 is changed by only 6 nm. (f) Simulated HRTEM image of Au and S atoms on a thin amorphous C film. The Au atoms (but not the S atoms) can be identified unambiguously from the image contrast.

3.3. Hole and terrace formation

Fig. 2 and Movies S1 - S2 show the formation and growth of holes as a result of thinning of the a-C film due to electron irradiation. Thinning of the C film is expected to take place at its exit surface, with an

estimated sputtering rate of 0.09 nm/s for the conditions used in our experiments (see Fig. S1 in the Supporting Information). The breaking of C-C bonds is likely to contribute to softening of the film, while electron-beam-induced thermal explosions of the hydrocarbon clusters that are typically present in C films can also create holes within them that can enlarge rapidly due to subsequent irradiation (Börrnert *et al.*, 2012). As the experiments were not carried out under ultra-high-vacuum conditions, O plasma etching of the a-C can also play an important role and can be enhanced by the presence of small amounts of carbonyl sulphide (Kim *et al.*, 2013). As the threshold energy for ejecting a C atom depends on its local bonding configuration, C atoms with dangling bonds at the edges of holes are easier to sputter and may contribute to the rapid growth of holes. Although catalytic etching by metal atoms can be an important mechanism of hole enlargement, this behavior was not observed for Au in the present study.

Fig. 2 and Movies S1 - S2 show that areas of the a-C film around holes exhibit graphitic terraces and monatomic steps. The transformation of a-C to graphitic C cannot be explained by preferential sputtering of the edges alone. S-induced graphitization may take place if S atoms are located interstitially between C layers. However, because the reaction between S and imperfect C is slow, this process requires rapid heating for S to evaporate without reaction and for C atoms to rearrange around the newly-formed defect (Brandtzeg and Øye, 1988). In our experiments, the specimen temperature is expected to be low, yet we still observe graphitization. We believe that electron-beam-induced reordering of a-C (Banhart, 1999; Börrnert *et al.*, 2012) takes place in the form of self-organization of glassy C into graphitic C. This is a well-known phenomenon, which results from cross-linking between neighbouring molecules at low temperature.

Such a transformation introduces local changes in density and has been used to explain the strain-induced enlargement of holes in a-C films under electron irradiation (Marquez-Lucero *et al.*, 2005). We propose that the presence of graphitic terraces at the sides of the holes in Fig. 2 and their subsequent enlargement is associated with the formation of graphitic lamellar domains in the a-C film, with the graphitic layers sliding across one another because of contraction of the C film, as shown schematically in Fig. 5.

This inference is important because a-C is one of the most lubricious materials known, but the mechanism for its lubricity is not well understood at the atomic level (Sanchez-López *et al.*, 2003). It has been predicted that tensile stress in a-C can reorient C-C bonds and induce the formation of lamellar domains of graphite, resulting in low friction originating from repulsive and low shear interactions across the sliding interface (Ma *et al.*, 2011).

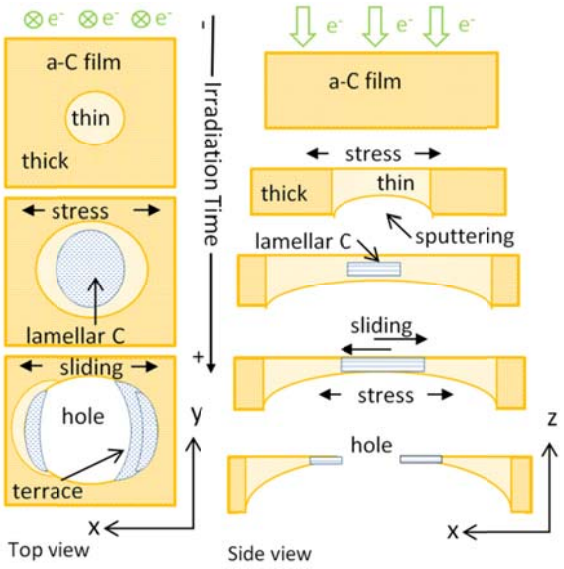

Fig. 5 Schematic diagram showing the proposed mechanism of formation of graphitic terraces. The electron beam sputters C atoms away from the exit surface of the a-C film. Graphite forms with a lamellar structure in the a-C as a result of shear strain. Holes enlarge rapidly as a result of sputtering at their edges, accompanied by sliding of the graphitic lamellae that form terraces on opposite sides of the hole.

3.4. Relationship between particle morphology and support film structure

In our experiments, we observe a clear relationship between the sizes of the Au clusters and the local structure of the C film, as summarized in Fig. 6. On a-C, Au clusters with sizes larger than 1.5 nm are found to be crystalline (Fig. 6a), while smaller clusters adopt more disordered three-dimensional configurations and undergo frequent atomic rearrangements (Fig. 6b). *Ab initio* calculations combined with aberration-corrected STEM images of mobile metal adatoms on single layer, bilayer and trilayer graphene have shown that migration barriers are very low for Au on graphene, with metal adatoms bonding preferentially where C-C bonds are stretched and that the electron density for forming new bonds with the adatoms is higher (Jensen *et al.* 2004; Batson, 2008; Zan *et al.*, 2011; Hardcastle *et al.*, 2013). We observe a greater affinity for clusters to bind to imperfect and strained regions around holes in the film and to the steps of terraces. Because of the active nature of low-coordinated particles, the cohesive energy may be overwhelmed by chemical bonding to the support, leading to substantial changes in atomic arrangement even for crystalline particles, as observed previously for Ge, Cr and Fe clusters (Bals *et al.*, 2012; Wang *et al.*, 2012b, 2013). For example, the Au particle in Fig. 6c adapts its structure to match the shape of the C edge. Fig. 6d shows an image detail taken from Movies S1 - S3, in which several atoms form a planar monolayer at the graphite edge. This observation is consistent with *ab initio* calculations, which predict that small Au clusters adopt planar structures for sizes of up to 15 atoms (Wang *et al.*, 2002). Fig. 6 shows that the terrace near the Au cluster is very likely to be graphene or very thin graphite, as confirmed by the hexagonal symmetry of the diffractogram and the spacings of the diffracted spots. The fact that clusters can bind strongly to the edge of the film also provides a template for the hexagonal ordering of Au atoms, as observed previously for planar Fe clusters on

graphene (Wang *et al.*, 2012b). We compared the HRTEM image of the cluster shown in Figs. 6d and 6e with multislice simulations. Fig. 6f shows three models of a cluster of 7 atoms of Au placed at a height of 0.3 nm above a graphene layer. This value is mid-way between that predicted theoretically (Vanin *et al.*, 2010) and without considering van der Waals interactions (Chan and Yim, 2013). The three models used in the calculations correspond to the binding of Au adatoms on three sites of high symmetry in graphene: a hollow (H) site at the center of a hexagon, a bridge (B) site at the midpoint of a C-C bond and a top (T) site above a C atom (Chan *et al.*, 2008). Figs. 6e and 6f show simulated HRTEM images generated for the imaging parameters given in Table S1. The best match to the experimental image is obtained for Au atoms on T-sites, for which the intensity maxima are located between the Au atoms in a 3-fold pattern, although it should be noted that the contrast features of single atoms in HRTEM images are very sensitive to the imaging conditions used (see Fig. 4). Interestingly, this result is in agreement with *ab initio* calculations performed by Brito and Miwa (2010) and with experimental results obtained using aberration-corrected HAADF STEM (Zan *et al.* 2011),

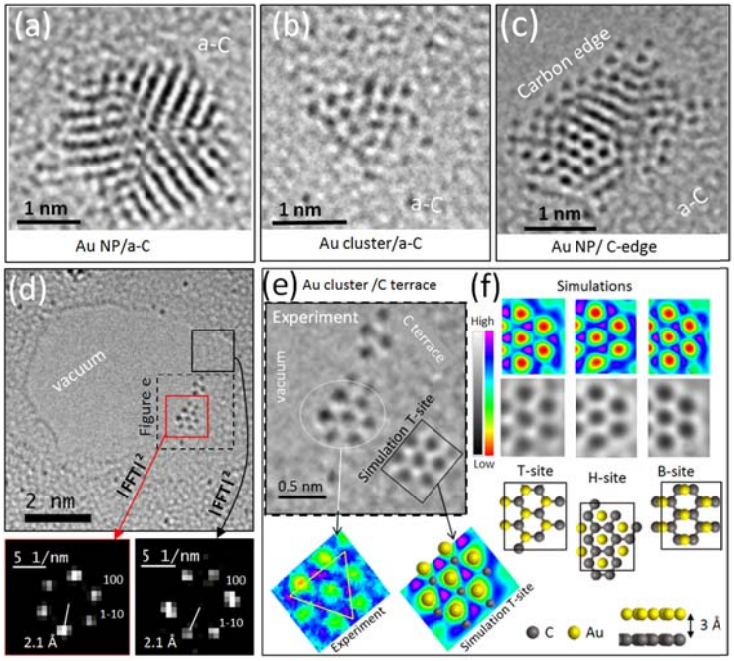

Fig. 6 Structures of thiol-protected Au clusters on different C allotropes. (a) Au clusters on a-C are typically crystalline for sizes above about 1.5 nm. (b) Ultrafine clusters below about 1 nm are disordered and three-dimensional (see Fig. 1), with frequent atomic rearrangements. (c) Au clusters interact strongly with the graphite edges and steps, adapting their shapes to the profiles of edges. (d) A cluster with several Au atoms adopts a planar shape and binds to the edge of a graphitic patch. Below are shown two diffractograms corresponding to the two areas inside the solid squares in (d). The symmetry and the spacings confirm that the terrace has the hexagonal structure of graphene. (e) Detail of the planar Au cluster shown inside the dashed square in (d). The inset shows a multislice simulation of the cluster, with Au atoms located on T-sites 0.3 nm above the graphene layer. (f) Atomistic models used for multislice simulations of Au atoms on B-, H- and T- sites. The simulated intensities are shown in false color (red=low and violet=high intensity).

Conclusions

High-resolution transmission electron microscopy has been used to provide insight into the equilibrium shapes of Au clusters capped with dodecanothiols supported on a-C films and to highlight the influence of both the C support and electron irradiation on their physical properties. Larger clusters on a-C are found to be crystalline and more equidimensional, while clusters with sizes below about 1.5 nm are more disordered. On graphitic layers, the clusters adopt elongated shapes along the edges and steps and planar arrangements when they contain only a few Au atoms. We illustrate the electron-beam-induced transformation of a-C into graphitic terraces, which suggests that C-C bond reorientation is mediated by electron-beam-induced shear strain.

Acknowledgements

LCG is grateful to Prof. Asunción Fernández for her leadership of the European project REGPOT-CT-2011-285895-Al-NANOFUNC, as well as to the European Union under a contract for an Integrated Infrastructure Initiative 312483 - ESTEEM2 for funding.

Supporting Information:

- Calculation of sputtering rate of a-C film under electron irradiation.
- Calculation of knock-on energies as a function of accelerating voltage.
- Table of published values of bonding and migration energies of Au and C atoms in several atomic configurations.
- Table of imaging parameters used during the experiments and for multislice simulations.
- Two Movies S1 and S2 of *in situ* TEM experiments of the dynamics of of thiol-protected Au clusters supported on an a-C film at an electron dose rate of 46 A/cm^2 (2.9x10^6 electrons/nm^{2}s). Chains of Au atoms and isolated Au atoms are observed at the edges of the particles. C terraces form at the edges of holes.
- Two Movies S3 and S4 showing details extracted from Movie S1 of planar clusters and the interaction of clusters with C edges.

References

Ajayan, P.M., Marks, L. D., 1989. Experimental evidence for quasimelting in small particles. *Phys. Rev. Lett.* 63(3), 279-282.

Alloyeau, D., Oikawa, T., Nelayah, J., Wang, G., Ricolleau, C. Following Ostwald ripening in nanoalloys by high-resolution imaging with single-atom chemical sensitivity, 2012. *Appl. Phys. Lett.* 101, 121920.

Bals, S., Van Aert, S., Romero, C.P., Lauwaet, K., Van Bael, M.J., Schoeters, B., Partoens, B., Yücelen, E., Lievens, P., Van Tendeloo, G., 2012. Atomic scale dynamics of ultrasmall germanium clusters. *Nat. Comm.* 3, 897-902.

Barnard, A.S., Young, N.P., Kirkland, A.I., Van Huis, M.A., Xu, H., 2009. Nanogold: a quantitative phase map. *ACS Nano* 3, 1431-1436.

Batson, P.E., 2008. Motion of gold atoms on carbon in the aberration-corrected STEM. *Microsc. Microanal.* 14, 89-97.

Booth, T.J., Pizzocchero, F., Andersen, H., Hansen, T.W., Wagner, J. B., Jinschek, J.R., Dunin-Borkowski, R.E., Hansen, O., Bøggild, P., 2011. Discrete dynamics of nanoparticle channelling in suspended graphene. *Nano Lett.* 11, 2689-2692.

Börrnert, F., Avdoshenko, S.M., Bachmatiuk, A., Ibrahim, I., Büchner, B., Cuniberti, G., Rümmeli, M.H., 2012. Amorphous carbon under 80 kV electron irradiation: A means to make or break graphene. *Adv. Mater.* 24, 5630-5635.

Boukhvalov, D.W., Katsnelson, M.I., 2009. Destruction of graphene bymetal adatoms. *Appl. Phys. Lett.* 95, 023109.

Brandtzeg, S.R., Øye, H.A., 1988. A possible mechanism of sulphur induced graphitization. *Carbon* 26, 163-168.

Brito, W.H., Miwa, R.H., 2010. Adsorption and diffusion of gold adatoms on graphene nanoribbons: An ab initio study. *Phys. Rev B*. 82, 045417.

Brust M., Walter M., Bethell D., Schiffrin D. J., Whyman R., 1994. Synthesis of thiol-derivatised gold nanoparticles in a two-phase liquid-liquid system. *J. Chem. Soc. Chem. Commun.* 7, 801-802.

Chan, K.T., Neaton, J.B., Cohen, M. L., 2008. First-principles study of metal adatom adsorption on graphene. *Phys. Rev. B* 77, 235430.

Chan, B., Yim W.-L., 2013. Accurate computation of cohesive energies for small to medium-sized gold clusters. *J. Chem. Theory Comput.* 9, 1964-1970.

Ciston, J., Kim, J.S., Haigh, S.J., Kirkland, A.I., Marks, L.D., 2011. Optimized conditions for imaging the effects of bonding charge density in electron microscopy. *Ultramicroscopy* 111, 901-911.

Cretu, A.V., Krasheninnikov, J.A., Rodríguez-Manzo, J.A., Sun, L., Nieminen, R.M., Banhart, F., 2010. Migration and localization of metal atoms on strained graphene. *Phys. Rev. Lett.* 105, 196102.

Cretu, A.V., Rodríguez-Manzo, J.A., Demortière, A., Banhart, F., 2012. Electron beam-induced formation and displacement of metal clusters on graphene, carbon nanotubes and amorphous carbon. *Carbon* 50, 259-264.

Daniel M.-C., Astruc, D., 2004. Gold nanoparticles: assembly, supramolecular chemistry, quantum-size-related properties, and applications toward biology, catalysis, and nanotechnology. *Chem. Rev.* 104, 293-346.

Egerton, R.F., Li, P., Malac, M., 2004. Radiation damage in the TEM and SEM. *Micron* 35, 399-409.

Gan, Y., Sun, L., Banhart, F. One- and two-dimensional diffusion of metal atoms in graphene. *Small* 2008, 4(5), 587-591.

Girit, Ç.Ö., Meyer, J.C., Erni, R., Rossell, M.D., Kisielowski, C., Yang, L., Park, C.-H., Crommie, M.F., Cohen, M.L., Louie, S.G., Zettl, A., 2009. Graphene at the Edge: Stability and Dynamics. *Science* 323, 1705-1708.

Gontard, L.C., Jinschek, J.R., Ou, H., Verbeeck, J., Dunin-Borkowski, R.E., 2012. Three-dimensional fabrication and characterisation of core-shell nano-columns using electron beam patterning of Ge-doped SiO_2. *Appl. Phys. Lett.* 100, 263113.

Gontard, L.C., Dunin-Borkowski, R.E., Fernández, A., Ozkaya, D., Kasama, T., 2014. Tomographic heating holder for in situ TEM: study of Pt/C and PtPd/Al_2O_3 catalysts as a function of temperature. *Microsc. Microanal.* 20(3), 982-990.

Häkkinen, H., 2012. The gold-sulfur interface at the nanoscale. *Nat. Chem.* 4, 443-455.

Hardcastle, T.P., Seabourne, C.R., Zan, R., Brydson, R.M. D., Bangert, U., Ramasse, Q.M., Novoselov, K.S., Scott, A.J., 2013. Mobile metal adatoms on single layer, bilayer, and trilayer graphene: An ab initio DFT study with van derWaals corrections correlated with electron microscopy data. *Phys. Rev. B* 87, 195430.

Howie, A., 2004. Hunting the Stobbs factor. *Ultramicroscopy* 98, 73-79.

Jensen, P., Blase, X., Ordejón, P., 2004. First principles study of gold adsorption and diffusion on graphite. *Surface Science*, 564, 173-178.

Kaushik A.P. and Clancy P., 2012. Explicit all-atom modeling of realistically sized ligand-capped nanocrystals. *J. Chem. Phys.* 136, 114702.

Kim, J.K., Cho, S.I., Kim, N.G., Jhon, M.S., Min, K.S., Kim, C.K., Yeom, G.Y., 2013. Study on the etching characteristics of amorphous carbon layer in oxygen plasma with carbonyl sulphide. *J. Vac. Sci. Technol. A* 31, 021301.

Krasheninnikov, A.V., Banhart, F., 2007. Engineering of nanostructured carbon materials with electron or ion beams. *Nat. Mater.* 6, 723-733.

Kuwauchi, Y., Takeda, S., Yoshida, H., Sun, K., Haruta, M., Kohno, H., 2013. Stepwise displacement of catalytically active gold nanoparticles on cerium oxide. *Nano Lett.* 13, 3073-3077.

Li, Y., Fan, X., Qi, J., Ji, J., Wang, S., Zhang, G., Zhang, F., 2010. Gold nanoparticles-graphene hybrids as active catalysts for Suzuki reaction. *Mater. Res. Bull.* 45, 1413-1418.

Luedtke, W.D., Landman, U., 1996. Structure, dynamics, and thermodynamics of passivated gold nanocrystallites and their assemblies. *J. Phys. Chem.* 100(32), 13323-13329.

Ma, T.-B., Hu, Y.-Z. Liang Xu, Wang, L.-F., Wang, H., 2011. Shear-induced lamellar ordering and interfacial sliding in amorphous carbon films: A superlow friction regime. *Chem. Phys. Lett.* 514, 325-329.

Meyer, J. C., Girit, Ç.Ö., Crommie, M.F., Zettl, A., 2008. Imaging and dynamics of light atoms and molecules on graphene. *Nature* 454, 319-322.

Meyer, J.C., Kurasch, S., Park, H. J., Skakalova, V., Künzel, D., Groß, A., Chuvilin, A., Algara-Siller, G., Roth, S., Iwasaki, T., Starke, U., Smet, J.H., Kaiser, U., 2011. Experimental analysis of charge redistribution due to chemical bonding by high-resolution transmission electron microscopy. *Nat. Mater.* 10, 209-215.

Márquez-Lucero, A., Gomez, J.A., Caudillo, R., Miki-Yoshida, M., Yacamán, M.J., 2005. Method to evaluate the tensile strength and stress-strain relationship of carbon nanofibers, carbon nanotubes, and C-chains. *Small* 1(6), 640-644.

Mariscal, M.M., Olmos-Asar, J.A., Gutierrez-Wing, C., Mayoral, A., Yacamán, M.J., 2010. On the atomic structure of thiol-protected gold nanoparticles: a combined experimental and theoretical study. *Phys. Chem. Chem. Phys.* 12, 11785-11790.

Ramasse, Q.M., Zan, R., Bangert, U., Boukhvalov, D.W., Son, Y.-W., Novoselov, K.S., 2012. Direct experimental evidence of metal-mediated etching of suspended graphene. *ACS Nano* 6, 4063-4071.

Saha, K, Agasti, S.S., Kim, C., Li, X., Rotello, V.M., 2012. Gold nanoparticles in chemical and biological sensing. *Chem. Rev.* 112, 2739-2779.

Sánchez-López, J.C., Erdemir, A., Donnet, C., Rojas, T.C., 2003. Friction-induced structural transformations of diamondlike carbon coatings under various atmospheres. *Surf. Coat. Technol.* 163-164, 444-450.

Smith, D.J., Petford-Long, A.K., Wallenberg, L.R., Bovin, J.O., 1986. Dynamic atomic-level rearrangements in small gold particles. *Science 233*, 872-875.

Vanin, M., Mortensen, J.J., Kelkkanen, A.K., Garcia-Lastra, J.M., Thygesen, K.S., Jacobsen, K.W., 2010. Graphene on metals: A van der Waals density functional study. *Phys. Rev. B* 81, 081408.

Wang, J., Wang, G., Zhao, J., 2002. Density-functional study of Au_n(n=2-20) clusters: Lowest-energy structures and electronic properties. *Phys. Rev. B* 66, 035418.

Wang, H., Li, K., Cheng, Y., Wang, Q., Yao, Y., Schwingenschlögl, U., Zhang, X.X., Yang, W., 2012a. Interaction between single gold atom and the graphene edge: A study via aberration-corrected transmission electron microscopy. *Nanoscale* 4, 2920-2925.

Wang, H., Li, K., Yao, Y., Wang, Q., Cheng, Y., Schwingenschlögl, U., Zhang, X.X., Yang, W., 2012b. Unraveling the atomic structure of ultrafine iron clusters. *Scientific Reports* 2, 995. doi: 10.1038/srep00995.

Wang, H., Feng, Q., Cheng, Y., Yao, Y., Wang, Q., Li, K., Schwingenschlögl, U., Zhang, X.X., Yang, W., 2013. Atomic bonding between metal and graphene. *J. Phys. Chem. C* 117, 4632-4638.

Wanner, M., Werner, R., Gerthsen, D., 2006. Dynamics of gold clusters on amorphous carbon films induced by annealing in a transmission electron microscope. *Surf. Sci.* 600, 632-640.

Werner, R., Wanner, M., Schneider, G., Gerthsen, D., 2005. Island formation and dynamics of gold clusters on amorphous carbon films. *Phys. Rev B* 72, 045426.

Williams P., 1987. Motion of small gold clusters in the electron microscope. *Appl. Phys. Lett.* 1987, 50, 1760-1762.

Yoshida, K., Bright, A., Tanaka, N., 2012. Direct observation of the initial process of Ostwald ripening using spherical aberration-corrected trasnmission electron microscopy. *J. Electron Microsc.* 61, 99-103.

Yoshida, K., Tominaga, T., Hanatani, T., Tagami, A., Sasaki, Y., Yamasaki, J., Saitoh, K., Tanaka, N., 2013. Key factors for the dynamic ETEM observation of single atoms. *Microscopy* 62, 571-582.

Zan, R., Bangert, U., Ramasse, Q., Novoselov, K.S., 2012. Interaction of metals with suspended graphene observed by transmission electron microscopy. *J. Phys. Chem. Lett.* 3, 953-958.

Zharnikov M., Geyer, W., Gölzhäuser, A., Frey, S., Grunze, M., 1999. Modification of alkanethiolate monolayers on Au-substrate by low energy electron irradiation : Alkyl chains and the S/Au interface. *Phys. Chem. Chem. Phys.* 1, 3163-3171.